

p53 induces formation of *NEAT1* lncRNA-containing paraspeckles that modulate replication stress response and chemosensitivity

Carmen Adriaens^{1,2,18}, Laura Standaert^{1,2,18}, Jasmine Barra^{1,2}, Mathilde Latil³, Annelien Verfaillie⁴, Peter Kalev^{5,6}, Bram Boeckx^{7,8}, Paul W G Wijnhoven⁹, Enrico Radaelli¹⁰, William Vermi^{11,12}, Eleonora Leucci^{1,2}, Gaëlle Lapouge³, Benjamin Beck³, Joost van den Oord¹³, Shinichi Nakagawa^{14,15}, Tetsuro Hirose¹⁶, Anna A Sablina^{5,6}, Diether Lambrechts^{7,8}, Stein Aerts⁴, Cédric Blanpain^{3,17} & Jean-Christophe Marine^{1,2}

In a search for mediators of the p53 tumor suppressor pathway, which induces pleiotropic and often antagonistic cellular responses, we identified the long noncoding RNA (lncRNA) *NEAT1*. *NEAT1* is an essential architectural component of paraspeckle nuclear bodies, whose pathophysiological relevance remains unclear. Activation of p53, pharmacologically or by oncogene-induced replication stress, stimulated the formation of paraspeckles in mouse and human cells. Silencing *Neat1* expression in mice, which prevents paraspeckle formation, sensitized preneoplastic cells to DNA-damage-induced cell death and impaired skin tumorigenesis. We provide mechanistic evidence that *NEAT1* promotes ATR signaling in response to replication stress and is thereby engaged in a negative feedback loop that attenuates oncogene-dependent activation of p53. *NEAT1* targeting in established human cancer cell lines induced synthetic lethality with genotoxic chemotherapeutics, including PARP inhibitors, and nongenotoxic activation of p53. This study establishes a key genetic link between *NEAT1* paraspeckles, p53 biology and tumorigenesis and identifies *NEAT1* as a promising target to enhance sensitivity of cancer cells to both chemotherapy and p53 reactivation therapy.

The p53 tumor suppressor is inactivated in most cancers through mutations in the *TP53* gene or via alternative mechanisms, such as overexpression of mouse double minute 2 (MDM2) or MDM4, which promote p53 degradation and/or inactivation of function¹. Tumors are addicted to loss of p53 function², and pharmacological reactivation of p53 has become a potential therapeutic strategy. The observation that Nutlin-3a, a small-molecule inhibitor of the p53–MDM2 interaction, triggers p53 activation and suppresses tumor growth in a *TP53* wild-type (WT) osteosarcoma murine xenograft model³ paved the way to the development of more potent and selective small-molecule inhibitors of MDM2, some of which are now in clinical development⁴.

However, the pleiotropic effects of p53 complicate p53 reactivation strategies. p53 triggers antagonistic cellular responses such as apoptotic cell death, senescence, reversible cell cycle arrest, DNA repair and autophagy. In contrast to activation of apoptosis, which helps to eliminate defective cells, induction of cell cycle arrest and the associated DNA repair program leads to cell survival⁵. The molecular

events that initiate p53-dependent cell cycle arrest (life) or apoptotic (death) transcriptional programs remain elusive. As MDM2 antagonists induce mainly G1 cell cycle arrest and apoptosis or senescence only rarely⁶, a clear understanding of the mechanisms that control cell fate determination by p53 may inform development of therapies to kill cancer cells more efficiently.

A putative contribution of the noncoding portion of the human genome in cell fate decision downstream of p53 has been largely underexplored. The noncoding genome is transcribed in vast numbers of RNA species, including lncRNAs⁷. Many lncRNAs have been suggested to regulate tumorigenesis on the basis of transfection studies and/or correlative expression analyses, although *Xist* (encoding X-inactive specific transcript) and *Malat1* (encoding metastasis-associated lung adenocarcinoma transcript 1) are the only two lncRNAs for which a clear genetic link with tumorigenesis has been established^{8,9}. Relevant to p53, several lncRNAs, including *NEAT1* (encoding nuclear paraspeckle assembly transcript 1), have already been identified as p53

¹Laboratory for Molecular Cancer Biology, Center for the Biology of Disease, VIB, KU Leuven, Leuven, Belgium. ²Laboratory for Molecular Cancer Biology, Center for Human Genetics, KU Leuven, Leuven, Belgium. ³Université Libre de Bruxelles, Institut de Recherche Interdisciplinaire en Biologie Humaine et Moléculaire, Bruxelles, Belgium. ⁴Laboratory of Computational Biology, Center for Human Genetics, KU Leuven, Leuven, Belgium. ⁵Laboratory for Mechanisms of Cell Transformation, Center for the Biology of Disease, VIB, KU Leuven, Leuven, Belgium. ⁶Laboratory for Mechanisms of Cell Transformation, Center for Human Genetics, KU Leuven, Leuven, Belgium. ⁷Vesalius Research Center, VIB, KU Leuven, Leuven, Belgium. ⁸Laboratory for Translational Genetics, Department of Oncology, KU Leuven, Leuven, Belgium. ⁹The Wellcome Trust/Cancer Research UK Gurdon Institute, University of Cambridge, Cambridge, UK. ¹⁰Mouse Histopathology Core Facility, Center for the Biology of Disease, VIB, KU Leuven, Leuven, Belgium. ¹¹Section of Pathology, Department of Molecular and Translational Medicine, University of Brescia, Brescia, Italy. ¹²Department of Pathology and Immunology, Washington University School of Medicine, St. Louis, Missouri, USA. ¹³Laboratory of Translational Cell and Tissue Research, Department of Pathology, KU Leuven and UZ Leuven, Leuven, Belgium. ¹⁴RNA Biology Laboratory, RIKEN, Wako, Japan. ¹⁵Faculty of Pharmaceutical Sciences, Hokkaido University, Sapporo, Japan. ¹⁶Institute for Genetic Medicine, Hokkaido University, Sapporo, Japan. ¹⁷WELBIO, Université Libre de Bruxelles, Bruxelles, Belgium. ¹⁸These authors contributed equally to this work. Correspondence should be addressed to J.-C.M. (jeanchristophe.marine@cme.vib-kuleuven.be).

Received 4 March; accepted 2 June; published online 4 July 2016; doi:10.1038/nm.4135

targets^{10–13}. Here we provide genetic evidence that *NEAT1* is engaged in a negative feedback loop with p53 and thereby modulates cancer formation in mice by dampening oncogene-dependent activation of p53. Consistent with this finding, *NEAT1* targeting sensitized established human cancer cells to both chemotherapy and p53 reactivation therapy. These data further illustrate the relevance of lncRNAs in tumorigenesis and their potential as therapeutic targets.

RESULTS

NEAT1 is a p53 target gene

To gain a comprehensive view of the p53 downstream signaling network, we established the transcriptome (RNA-seq) and genome-wide occupancy of p53 (chromatin immunoprecipitation sequencing (ChIP-seq)) in *TP53* WT MCF-7 breast cancer cells exposed to Nutlin-3a to stabilize p53 (ref. 14). We identified 110 and 147 annotated lncRNAs that were downregulated and upregulated, respectively, in cells treated with Nutlin-3a ($|\log_2$ fold change (FC)| > 1, adjusted $P < 0.05$). To determine which of these transcripts are bona fide p53 targets, we searched for p53-binding sites within 10 kb upstream and downstream of their transcription start sites (TSS) by adapting the i-cisTarget method¹⁵. The p53-responsive element was the most significantly enriched motif within the upregulated genes, whereas it was undetectable among the downregulated loci. Among 73 loci in which at least one p53-binding motif was identified, 16 exhibited p53 ChIP-seq peak(s) within 10 kb of their TSS (Supplementary Table 1 and Supplementary Fig. 1). We curated this list for reliability of the annotation and identified five lncRNA genes likely to be direct p53 targets (Supplementary Table 1 and Supplementary Fig. 1).

One of these, *NEAT1*, was previously reported to be induced by p53 (ref. 13) and is required for the assembly of subnuclear bodies known as paraspeckles¹⁶. Indeed, we observed a p53 ChIP-seq peak upstream of the *NEAT1* promoter and significant ($P = 5.314 \times 10^{-11}$) induction of the 3.7-kb polyadenylated *NEAT1* transcript (*NEAT1_1*) in Nutlin-3a-treated cells (Fig. 1a and Supplementary Fig. 2a), indicating that *NEAT1* is a direct p53 target gene.

In addition to the 3.7-kb transcript, *NEAT1* produces a long (21.7 kb) isoform (*NEAT1_2*). This transcript is not polyadenylated¹⁷ (Supplementary Fig. 2b) and, accordingly, was not detected in our poly(A)+ RNA-seq data sets. Although both *NEAT1_1* and *NEAT1_2* are present in paraspeckles, their formation is strictly dependent on *NEAT1_2* (refs. 16,18–20). To assess whether *NEAT1_2* is also induced by p53, we quantified its expression by RT-qPCR in cells exposed to Nutlin-3a. We generated cDNA using random hexamers (instead of oligo-dTs) to amplify both *NEAT1* isoforms. Because these overlap completely at the 5' end, primer pair A detects both isoforms, whereas primer pair B detects *NEAT1_2* specifically (Supplementary Fig. 2b). Both total *NEAT1* and *NEAT1_2* were induced in human *TP53* WT MCF-7, NGP, HCT116 and U2OS cells but not in MCF-7 or NGP cells expressing small hairpin RNAs (shRNAs) targeting *TP53* (shTP53), *TP53* knockout (KO) HCT116 cells or *TP53* mutant MM118 cancer cells (Fig. 1b–f). Induction of the p53-target gene *CDKN1A* confirmed activation of p53 in all *TP53* WT Nutlin-3a-treated cells (Fig. 1b–f). Expression of *NEAT1* and *NEAT1_2* was also induced in normal human embryonic cells (hES), immortalized fibroblasts (BJ) and low-passage mouse embryonic fibroblasts (MEFs) exposed to Nutlin-3a (Fig. 1g and Supplementary Fig. 2c,d).

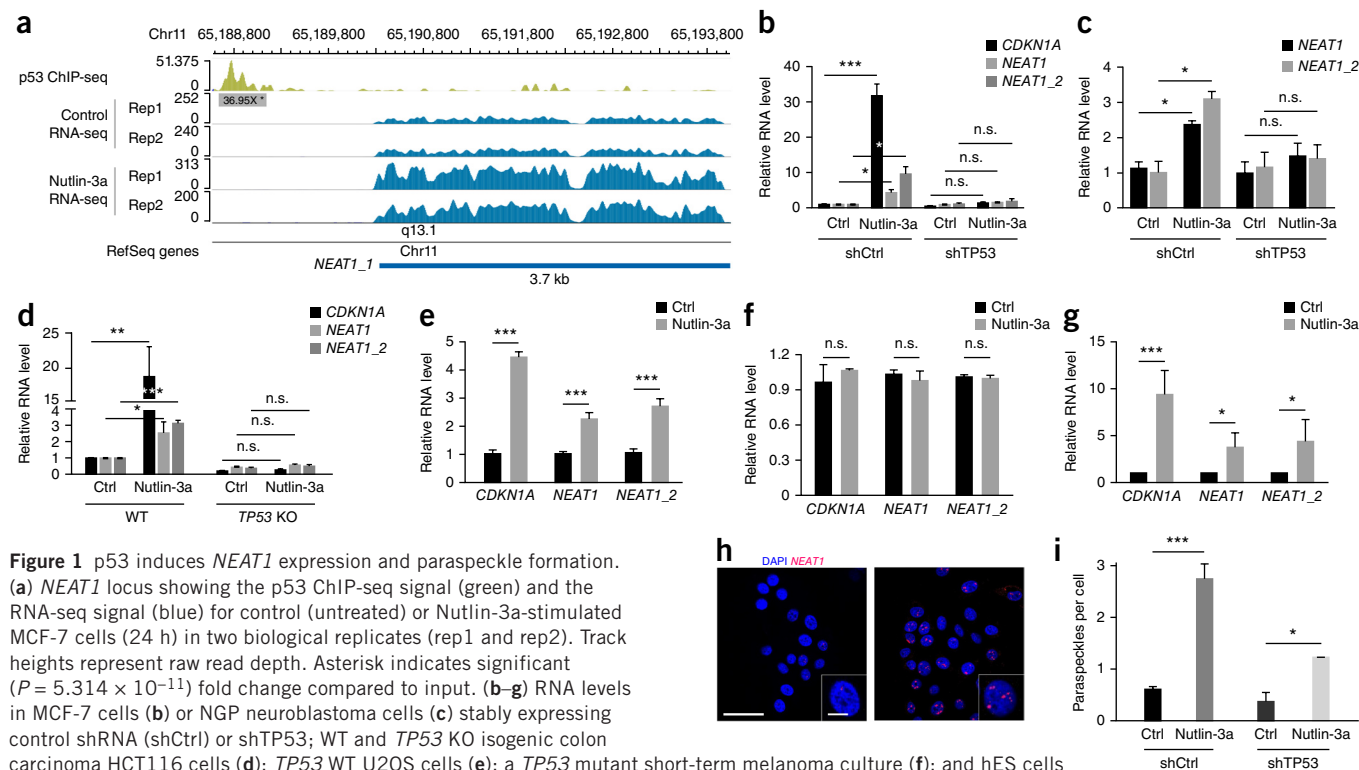


Figure 1 p53 induces *NEAT1* expression and paraspeckle formation. (a) *NEAT1* locus showing the p53 ChIP-seq signal (green) and the RNA-seq signal (blue) for control (untreated) or Nutlin-3a-stimulated MCF-7 cells (24 h) in two biological replicates (rep1 and rep2). Track heights represent raw read depth. Asterisk indicates significant ($P = 5.314 \times 10^{-11}$) fold change compared to input. (b–g) RNA levels in MCF-7 cells (b) or NGP neuroblastoma cells (c) stably expressing control shRNA (shCtrl) or shTP53; WT and *TP53* KO isogenic colon carcinoma HCT116 cells (d); *TP53* WT U2OS cells (e); a *TP53* mutant short-term melanoma culture (f); and hES cells (g) exposed to Nutlin-3a (5 μ M) for 24 h. Values are normalized to the levels of RNA expression in untreated cells, was set to 1. Error bars, mean \pm s.e.m. ($n = 3$ (b,f) 2 (c), 5 (d), 6 (e) or 4 (g) biological replicates). (h) Confocal images after *NEAT1* RNA-FISH (red) with nuclear DAPI counterstain (blue) in MCF-7 cells treated with vehicle (left) or Nutlin-3a (right). Scale bars, 50 μ m (main) and 12.5 μ m (inset). (i) Quantification of paraspeckles as determined by RNA-FISH in shCtrl and shTP53 MCF-7 cells, untreated (ctrl) or treated with Nutlin-3a. Data are mean \pm s.d. of two biological replicates. * $P < 0.05$; ** $P < 0.01$ and *** $P < 0.001$, unpaired two-sided t -tests (b,c,e–h) or Mann-Whitney U -test (d).

p53 induces paraspeckle formation

Assembly of paraspeckles, which is dependent on *NEAT1_2* expression, is thought to widely affect gene expression via distinct mechanisms²¹. Because p53 stimulates *NEAT1_2* expression, we asked whether p53 can promote paraspeckle formation using *NEAT1_2* RNA–fluorescence *in situ* hybridization (RNA–FISH). We observed a marked increase in the *NEAT1_2* RNA–FISH signal, which was distributed in a characteristic punctate pattern, in MCF-7 cells after treatment with Nutlin-3a. This increase was attenuated in MCF-7 cells expressing *TP53*-targeting shRNAs (Fig. 1h,i) but was not completely abrogated, as silencing of *TP53* was not complete (data not shown). Likewise, human diploid fibroblasts (BJ cells) and *TP53* WT HCT116 cells showed increased numbers of paraspeckles upon Nutlin-3a exposure, but BJ cells expressing shTP53 and isogenic *TP53* KO HCT116 cells did not (Supplementary Fig. 2e,f). We conclude that pharmacological activation of p53 stimulates paraspeckle formation.

Oncogenic stimuli induce *NEAT1* paraspeckle formation *in vivo*

p53 is induced by a variety of stress signals, many of which activate, either directly or indirectly, the DNA-damage response (DDR)²². Such signals include exposure to the DNA-damaging agent doxorubicin; increases in reactive oxygen species (ROS) owing to treatment with the mitochondrial uncoupler rotenone or passaging in nonphysiological O₂ levels; and telomere attrition upon long-term culturing. We observed induction of *NEAT1* and *NEAT1_2* expression in all these experimental conditions, in both cancer cell lines (i.e., MCF-7) and immortalized diploid fibroblasts (WI38 and BJ cells) and this induction was accompanied by an increase in paraspeckle formation (Fig. 2a–c and Supplementary Fig. 3a–c). *NEAT1* and *NEAT1_2* were induced in parental MCF-7 cells exposed to doxorubicin, but this

increase was attenuated in cells expressing shTP53 (Fig. 2a). Hence, expression of *NEAT1* and *NEAT1_2* is induced upon DNA damage, and this induction is at least partly p53 dependent.

The specific physiological conditions under which paraspeckles form *in vivo* are still unclear. We assessed whether paraspeckles are assembled in the epidermis of mice exposed to DMBA, a carcinogen known to induce p53. Whereas paraspeckles were barely detectable in the skin of untreated mice, we detected them after one dose of DMBA in WT (Fig. 2d,e) but not *Neat1* KO mice (Supplementary Fig. 3d), and the number of paraspeckle-positive cells increased after the second DMBA application (Fig. 2d). Mice were also exposed to the proinflammatory agent TPA at day 4. However, TPA exposure alone did not induce paraspeckle assembly (Supplementary Fig. 3e), indicating that the latter is a consequence of DMBA-induced genotoxic stress and not TPA-induced inflammation. To test whether DMBA-induced paraspeckle formation depends on the presence of functional p53, we exposed *Trp53* KO mice to the DMBA–TPA protocol. The number and intensity of the *Neat1* foci were substantially higher in *Trp53* WT than in *Trp53* KO tissues (Fig. 2e). Genotoxic stress, therefore, induces *Neat1* expression and paraspeckle formation *in vivo* in a p53-dependent manner.

Oncogene activation also induces p53 by engaging the ARF–MDM2 pathway and a DNA replication stress response²². In the two-stage DMBA and TPA carcinogenesis protocol, after the initial and transient DMBA-induced DDR, TPA administration results in a progressive selection of cells carrying oncogenic *Ras* mutations²³. Paraspeckle-positive cells were absent from untreated epidermis but readily detectable in hyperplastic interfollicular epidermis 1 week after DMBA–TPA administration and in differentiated K1-positive cells from benign skin tumors (papillomas) (Fig. 2f). Paraspeckle-positive

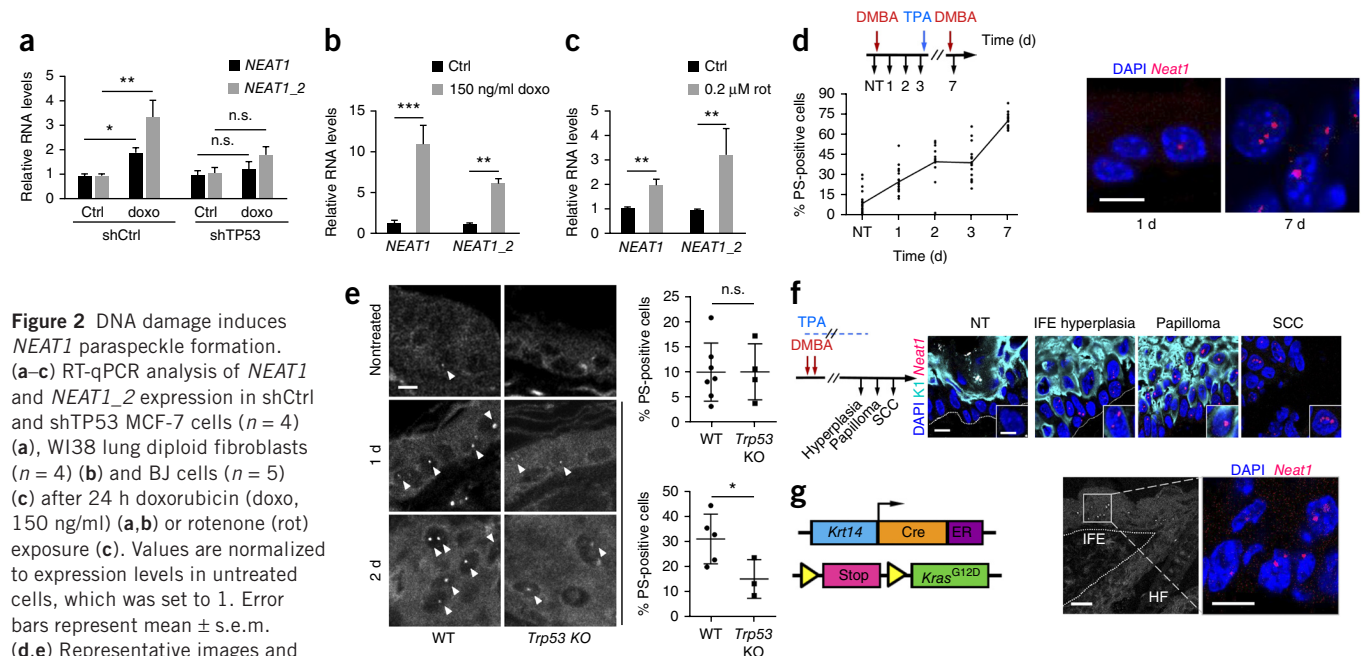
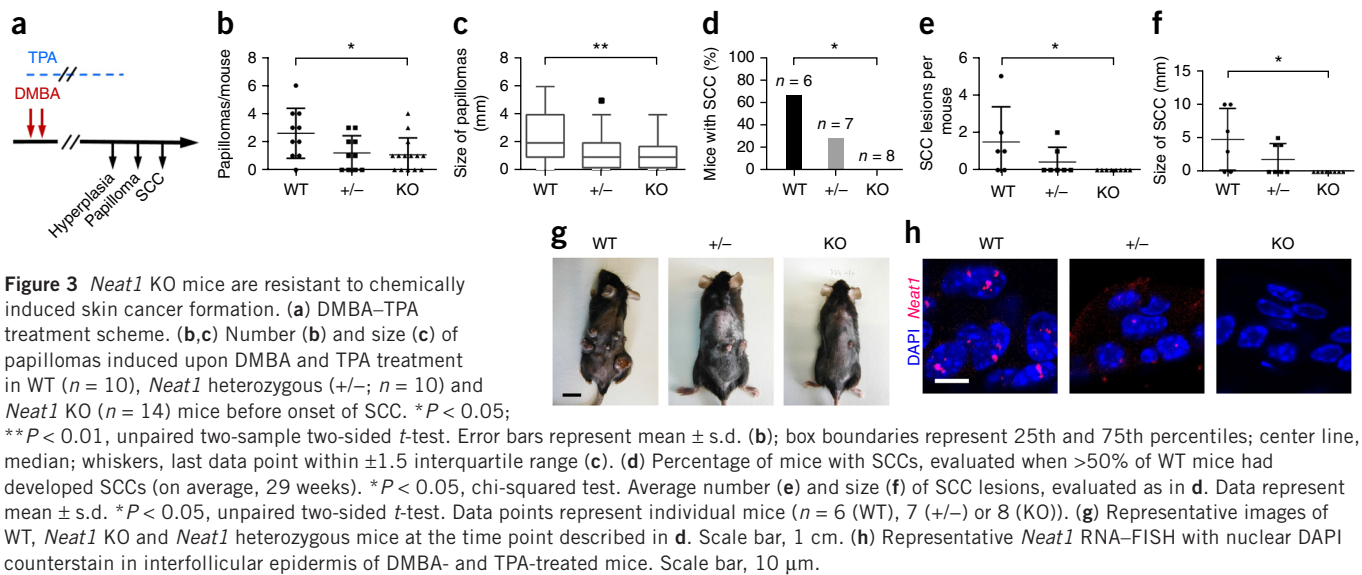


Figure 2 DNA damage induces *NEAT1* paraspeckle formation. (a–c) RT-qPCR analysis of *NEAT1* and *NEAT1_2* expression in shCtrl and shTP53 MCF-7 cells ($n = 4$) (a), WI38 lung diploid fibroblasts ($n = 4$) (b) and BJ cells ($n = 5$) (c) after 24 h doxorubicin (doxo, 150 ng/ml) (a,b) or rotenone (rot) exposure (c). Values are normalized to expression levels in untreated cells, which was set to 1. Error bars represent mean \pm s.e.m. (d,e) Representative images and

quantification of paraspeckle (PS) formation, assessed by *Neat1* RNA–FISH with DAPI counterstain in the skin of WT and *Trp53* KO mice exposed to DMBA and TPA. In d, dots represent individually quantified images of $n = 7$ (not treated (NT)), 3 (1, 3, 7 d) or 2 (2 d) mice per time point. In e, error bars represent mean \pm s.d. of $n = 7$ and 4 mice (top) or 5 and 3 (bottom). Scale bars, 10 μm. White arrowheads in e indicate paraspeckles. (f,g) Chemical (f, left) or genetic (g, left) strategies used to induce skin carcinogenesis and RNA–FISH of *Neat1* (red) with immunostaining for cytokeratin 1 (K1) and nuclear counterstain (DAPI) in skin from mice exposed to DMBA and TPA (f, right) or expressing oncogenic *Kras* (g, right). Scale bars, 10 μm (f, main), 5 μm (f, inset), 40 μm (g, main) and 10 μm (g, inset). IFE, interfollicular epidermis; SCC, squamous cell carcinoma; HF, hair follicle; n.s., not significant; * $P < 0.05$; ** $P < 0.01$; *** $P < 0.001$, unpaired two-sided *t*-test.



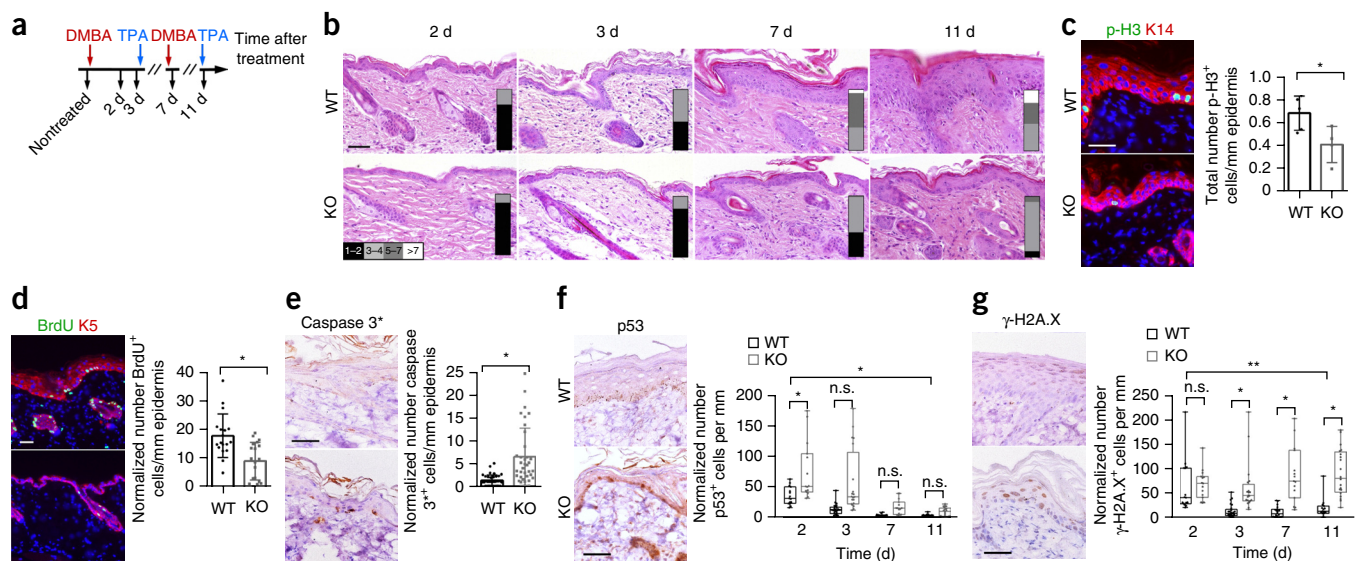
cells were also observed in roughly half of the lesions that progressed into malignant squamous cell carcinoma (SCC) (Fig. 2f).

To rule out the possibility that paraspeckle formation is specific to carcinogen-induced tumorigenesis, we measured paraspeckles in a genetically induced skin cancer mouse model²⁴. We crossed mice bearing an oncogenic *Kras*^{G12D} allele silenced by an upstream *loxP*-flanked (floxed) transcriptional stop cassette (*Kras*^{LSL-G12D}) with mice bearing a tamoxifen-inducible Cre allele driven by the keratin 14 (*K14*) promoter. Analysis of skin from TAM-exposed *Kras*^{G12D} knock-in, but

not wild-type (WT), mice showed the presence of paraspeckles in skin hyperplasias and papillomas (Fig. 2g and Supplementary Fig. 3f). Paraspeckle assembly is therefore induced in response to oncogene activation and is maintained as tumors are established and progress.

Neat1 promotes skin tumor formation

The presence of paraspeckles during the early stages of carcinogenesis prompted us to determine whether genetic inactivation of *Neat1* modulates tumor formation. We used previously described mice in



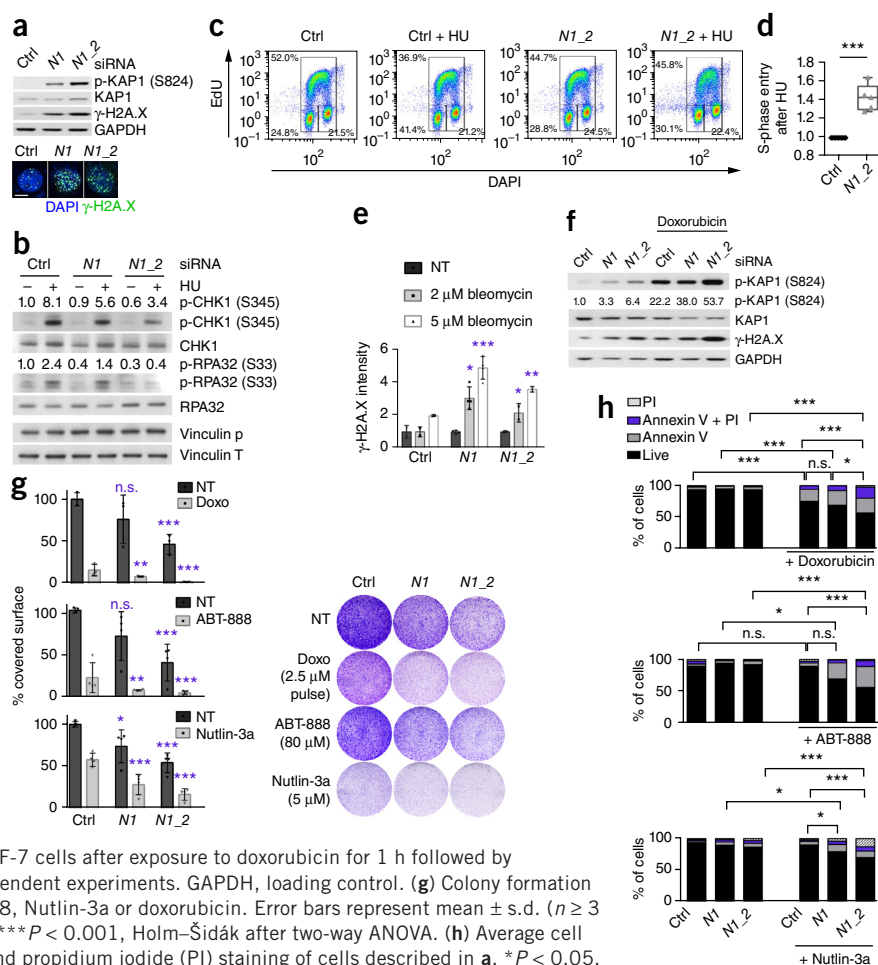
not wild-type (WT), mice showed the presence of paraspeckles in skin hyperplasias and papillomas (Fig. 2g and Supplementary Fig. 3f). Paraspeckle assembly is therefore induced in response to oncogene activation and is maintained as tumors are established and progress.

Neat1 promotes skin tumor formation

The presence of paraspeckles during the early stages of carcinogenesis prompted us to determine whether genetic inactivation of *Neat1* modulates tumor formation. We used previously described mice in

Figure 5 *NEAT1* paraspeckles modulate ATR signaling and chemosensitivity.

(a) Immunoblot analysis of the indicated proteins (top) and immunofluorescence images of γ -H2A.X and nuclear DAPI (bottom) in *NEAT1* (*N1*) KD and *NEAT1_2* (*N1_2*) KD MCF-7 cells. GAPDH, loading control. p-, phosphorylated; ctrl, siCtrl pools. Scale bar, 10 μ m. Representative images of three independent experiments. (b) Immunoblot analysis and quantification relative to siCtrl of p-CHK1 at S345 and p-RPA32 at S33 in *N1* KD and *N1_2* KD U2OS cells exposed to HU (1 mM). Phosphorylated (p) and total (T) vinculin were used as loading controls. Representative images of five independent experiments. (c,d) FACS analysis (c) and quantification of S-phase entry (d) after pulsing with EdU of siCtrl (ctrl) and *N1_2* KD U2OS cells with or without HU exposure (1 mM for 5 h). *** $P < 0.001$, unpaired two-sided t -test ($n = 5$). Box boundaries represent 25th and 75th percentiles; whiskers, minimum and maximum; center line, median. Representative data from five independent experiments. (e) Quantification of γ -H2A.X staining in ASO (ctrl), *N1* KD and *N1_2* KD U2OS cells after a 1 h exposure to bleomycin and a 24 h recovery period. NT, not treated. Error bars represent mean \pm s.d. * $P < 0.05$, ** $P < 0.01$, *** $P < 0.001$, two-way ANOVA with Šidák post-test correcting for multiple comparisons. Data are from two independent experiments. (f) Immunoblot analysis of *N1* KD and *N1_2* KD MCF-7 cells after exposure to doxorubicin for 1 h followed by 24-h recovery. Representative images of three independent experiments. GAPDH, loading control. (g) Colony formation assays using cells described in a exposed to ABT-888, Nutlin-3a or doxorubicin. Error bars represent mean \pm s.d. ($n \geq 3$ independent experiments). * $P < 0.05$, ** $P < 0.01$, *** $P < 0.001$, Holm-Šidák after two-way ANOVA. (h) Average cell viability using a FACS-based assay with annexin V and propidium iodide (PI) staining of cells described in a. * $P < 0.05$, *** $P < 0.001$, two-way ANOVA and Tukey's *post hoc* test ($n = 3$ independent experiments). Doxo, doxorubicin; n.s., not significant. Uncropped, unmodified images of gels are shown in **Supplementary Figure 8**.



which the *Neat1* locus is silenced by insertion of a transcriptional stop cassette upstream of its TSS²⁵ (**Supplementary Fig. 4a**). We exposed these *Neat1* KO mice, which are viable and healthy²⁵, to DMBA and TPA and quantified benign papillomas and invasive SCC (**Fig. 3**). Fewer and smaller papillomas were observed before the onset of SCC formation in *Neat1* KO and heterozygous mice compared with WT controls (**Fig. 3a–c**). When more than 50% of the WT mice had developed invasive skin lesions, none of the *Neat1* KO mice showed SCC (**Fig. 3d–f**), indicating that *Neat1* is required for tumor progression. *Neat1* haploinsufficiency also decreased the number and size of DMBA- and TPA-induced SCC (**Fig. 3d–f**). DMBA-TPA-induced paraspeckle formation was abolished in *Neat1* KO mice and compromised in *Neat1* heterozygous mice (**Fig. 3h**).

Neat1 prevents accumulation of DNA damage

WT mice treated with DMBA-TPA showed diffuse hyperplasia on day 7 and severe hyperplasia on day 11, after two applications of DMBA. In contrast, *Neat1* KO mice showed no hyperplasia on day 7 and only mild focal hyperplasia on day 11 (**Fig. 4a,b**). Keratinocyte proliferation was lower after DMBA exposure in *Neat1* KO mice than in WT mice (**Fig. 4c,d**). In addition, we observed a transient apoptotic response in keratinocytes of WT mice after the first DMBA application until the first TPA administration (**Fig. 4a**). In contrast, apoptosis was sustained for up to 11 d after the start of the

treatment in *Neat1* KO mice (**Fig. 4e**). Differences in cell proliferation and viability were significant only after the second DMBA application (**Supplementary Fig. 4b–e**).

p53 stabilization after DMBA administration was more pronounced and persistent in *Neat1* KO mice than in WT mice (**Fig. 4f**). Similarly, the number of cells expressing the DNA damage marker histone 2A.X phosphorylated at S139 (γ -H2A.X) decreased in WT mice 2 to 3 d after DMBA exposure but continued to increase in *Neat1* KO mice 3, 7 and 11 d after treatment (**Fig. 4g**). These results indicate that *Neat1* prevents accumulation of excessive DNA damage and concomitant activation of p53 in cells after DMBA-induced oncogenic stress.

NEAT1 depletion causes replication stress

We next asked whether *NEAT1* silencing leads to accumulation of DNA damage in established human cancer cells, which are by definition subject to oncogenic stress. To minimize confounding off-target effects, we silenced the *NEAT1_1* and *NEAT1_2* isoforms together or the long isoform (*NEAT1_2*) alone using both small interfering RNAs (siRNAs) and locked nucleic acid-modified antisense oligonucleotides (ASOs), which trigger RNase-H-mediated degradation of the target transcript upon ASO binding. We observed similar knockdown efficiencies and biological responses between these approaches (**Supplementary Fig. 5b,c**). Silencing of both *NEAT1* isoforms or of *NEAT1_2* alone in MCF-7 cells led to progressive increases in γ -H2A.X levels, foci

Figure 6 Detection of *NEAT1* paraspeckles in human cancers and correlation of *NEAT1_2* levels with response to platinum-based therapy. (a) Representative images of a series of paraspeckle-positive cases as assessed by *NEAT1* RNA-FISH, with normal skin shown as a negative control. Scale bars, 20 μ m (main) and 8 μ m (inset). Three representative images per case were collected; 97 cases from 24 different tumor types were analyzed (further details are presented in **Supplementary Table 2**). (b–d) Kaplan–Meier curves for PFS correlation with *NEAT1_1* and *NEAT1_2* expression levels in a cohort of primary high-grade ovarian carcinoma patients³¹ (b, d) and in the TCGA cohort³² (c) treated with platinum-based antineoplastic agents. CI, confidence interval.

formation and DDR signaling as indicated by an increase in phosphorylation of the ATM substrate KAP1 at S824 (**Fig. 5a**).

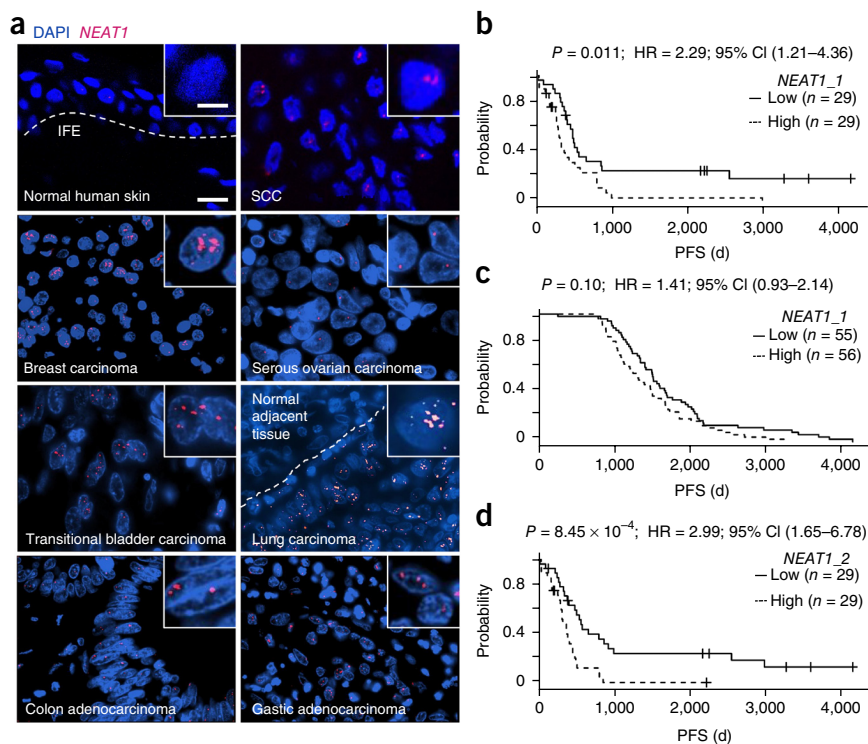
Oncogenes induce DNA hyper-replication, which causes replication fork stalling²⁶. Sophisticated mitotic and S-phase checkpoint pathways have evolved to ensure replication completion and prevent replication fork collapse, which leads to double-strand break (DSB) formation and possibly cell death. Activation of the kinase ATR prevents formation of DSBs in response to replication stress²⁶. To assess whether *NEAT1* paraspeckles modulate this critical survival pathway, we knocked down *NEAT1* in U2OS cells in which replication fork stalling was exacerbated by hydroxyurea (HU), an agent that blocks DNA synthesis²⁷. ATR signaling was compromised in *NEAT1* and *NEAT1_2* knockdown (KD) cells exposed to HU, as evidenced by a decrease in ATR-mediated phosphorylation of checkpoint kinase CHK1 at S345 and replication protein RPA32 at S33 (**Fig. 5b**).

Engagement of the ATR–CHK1 pathway activates G2–M and intra-S-phase checkpoints; failure of either step leads to replication fork collapse and formation of DSBs²⁸. The cell cycle profile of *NEAT1_2* KD cells was only moderately affected in the absence of HU (**Fig. 5c,d**). In contrast, progression through S phase was severely compromised in cells expressing control siRNA (siCtrl), whereas *NEAT1_2* KD cells continued to progress through S phase in the presence of HU (**Fig. 5c,d**). *NEAT1_2* is therefore essential for activation of ATR signaling and checkpoint activation in response to replication stress.

NEAT1 targeting sensitizes cancer cells to chemotherapy

Many chemotherapeutic agents cause DNA damage in replicating cells and thereby enhance replication stress²⁶. The above results suggest that *NEAT1_2* targeting may increase the sensitivity of human cancer cells to genotoxic chemotherapeutics. Consistently, we detected significantly higher amounts of γ -H2A.X foci in *NEAT1* KD and *NEAT1_2* KD U2OS cells exposed to a 1-h pulse of bleomycin than in cells treated with control ASOs (**Fig. 5e**). Similarly, the increase in phosphorylated KAP1 and γ -H2A.X levels and foci formation observed in *NEAT1* KD and *NEAT1_2* KD MCF-7 cells (**Fig. 5a**) was exacerbated upon doxorubicin exposure (**Fig. 5f**). Knockdown of *NEAT1* caused a marked decrease in cell growth and viability (**Fig. 5g,h**).

Poly(ADP-ribose) polymerase (PARP) inhibitors also enhance replication stress²⁹. Consistently, knockdown of *NEAT1* or *NEAT1_2* increased cancer cells' vulnerability to the potent PARP inhibitor ABT-888 (**Fig. 5g,h**). We obtained similar results in MCF-7 cells



treated with shTP53 and in the *TP53* mutant SCC cell line SQD9 (data not shown).

Silencing of *NEAT1* or *NEAT1_2* also increased Nutlin-3a-induced cytotoxicity (**Fig. 5g,h**), consistent with the idea that increased DNA damage sensitizes cells to p53 reactivation therapy³⁰. *NEAT1* targeting is therefore a promising strategy to enhance the effectiveness of DNA-damaging chemotherapeutics and p53 reactivating agents.

NEAT1_2 expression levels predict chemotherapy response

To assess whether paraspeckles are assembled in human primary cancers, we performed *NEAT1* RNA-FISH on a tissue microarray (TMA) containing 97 specimens of diverse origins (**Supplementary Table 2**). Consistent with the absence of paraspeckles in the majority of normal adult tissues in mice²⁵, the non-neoplastic component in the TMA core, which includes normal resident and stromal cells, systematically showed no paraspeckle formation (**Fig. 6a** and **Supplementary Fig. 6a**). We confirmed the absence of paraspeckles in additional normal skin and breast tissue samples (**Fig. 6a** and **Supplementary Fig. 6b**). In contrast, we detected paraspeckles in about 65% of the human carcinomas analyzed, including skin SCC and ovarian carcinomas (**Fig. 6a**, **Supplementary Fig. 6a,b** and **Supplementary Table 2**).

To evaluate whether *NEAT1* expression levels correlate with response to chemotherapy, we chose a cohort of primary high-grade ovarian carcinoma patients³¹ (GEO GSE30161), because all patients included in the cohort had been exposed to a first-line platinum-based chemotherapy, and expression data were available (owing to the presence of specific Affymetrix probes) for both *NEAT1_1* and *NEAT1_2*. When we correlated the expression levels of *NEAT1_1* with progression-free survival (PFS), correcting for race, disease stage, age and histology, we found that the correlation was not significant when considering a significance threshold of 0.01 ($P = 0.011$; **Fig. 6b**). We performed a similar analysis using the ovarian cancer cohort from the Cancer Genome Atlas³² (TCGA), for which expression data were available only for the polyadenylated *NEAT1_1* transcript. To obtain

a patient population comparable to the high-grade ovarian carcinoma cohort (Fig. 6b), we included only patients who had grade 2–3 serous ovarian cancers treated with first-line platinum-based chemotherapy and for whom recurrence data were available. This analysis confirmed that *NEAT1_1* expression is a poor predictor of chemotherapy response (Fig. 6c). In contrast, we observed a significant correlation between expression levels of *NEAT1_2* and PFS in the high-grade ovarian carcinoma data set (hazard ratio (HR) = 2.99, $P = 8.45 \times 10^{-4}$; Fig. 6d). On the basis of the analysis of this data set, it appears that expression of *NEAT1_2* but not *NEAT1_1* reliably predicts response of ovarian cancer to platinum-based chemotherapy.

DISCUSSION

We demonstrate here that the lncRNA *NEAT1* enables tumorigenesis *in vivo* by promoting the survival of oncogene-targeted cells. Although recent studies have indicated that *NEAT1* can promote the growth and survival of *in vitro*-cultured cancer cells^{33,34} and that high *NEAT1* levels correlate with poor prognosis in various types of cancer^{35–37}, our data establish the first clear genetic link between *NEAT1* and carcinogenesis.

Consistent with published reports¹³, we provide evidence that *NEAT1* is a bona fide p53 target gene. Moreover, we show that activation of p53 stimulates the formation of *NEAT1* paraspeckles. Our work therefore establishes a direct functional link between p53 and paraspeckle biology. There is growing evidence that paraspeckles regulate gene expression through a number of mechanisms, including sequestration of specific transcription factors and/or hyperedited mRNAs²¹. Consequently, activation of this regulatory program downstream of p53 may profoundly influence p53-mediated biological responses and, importantly, influence cell fate decisions downstream of p53.

The role of p53 as the ‘guardian’ of the genome has long been recognized. p53 can modulate virtually all DNA repair processes by both transcription-dependent and independent mechanisms³⁸. The observation that p53 induces *NEAT1* paraspeckle formation, which prevents the accumulation of excessive DNA damage in cells undergoing replication stress, reveals yet another route through which p53 preserves genomic integrity. Activation of the p53 network sets in motion an elaborate process of autoregulatory positive and negative feedback loops³⁹. Our findings that p53 regulates *NEAT1* expression to stimulate paraspeckle formation and that *NEAT1* paraspeckles, in turn, dampen replication-associated DNA damage and p53 activation reveal an autoregulatory negative feedback loop that attenuates p53 activity in DNA-damaged cells.

Mechanistically, we provide evidence that *NEAT1_2* preserves genomic integrity and viability of preneoplastic cells by modulating ATR signaling. This pathway is crucial for ensuring replication completion and in preventing replication fork breakage in cells undergoing replication stress. Accordingly, ATR or CHK1 deficiency compromises the viability of cells undergoing oncogene-induced replication stress²⁶. We therefore propose a model in which paraspeckle assembly is one of the mechanisms employed by preneoplastic cells to cope with oncogene-induced replication fork stalling and, ultimately, prevent accumulation of replication fork breakage and the deleterious consequences associated with excessive DSBs.

The precise molecular mechanisms underlying the role of *NEAT1* in ATR–CHK1 signaling remain to be elucidated. We show that specific silencing of the *NEAT1_2* isoform is sufficient to reduce ATR signaling, which indicates that proper ATR activation may depend on *NEAT1_2*-mediated paraspeckle assembly. It is possible that paraspeckles promote the retention or sequestration of proteins directly involved in the termination of the ATR–CHK1 response (such as

WT p53-induced phosphatase 1 or protein phosphatase 2A family phosphatases)^{40–42}. Alternatively, paraspeckles may act upstream of ATR–CHK1 signaling by decreasing the ability of oncogenes to induce hyper-replication by, for instance, controlling the availability of key replication factors and thereby limiting the firing of additional replication forks. Paraspeckles may also function as a site of activation (for example, through induction of specific post-translational modifications) of proteins that contribute to ATR–CHK1 activation.

In addition to its role in ATR signaling, *NEAT1_2* and/or paraspeckles may also contribute to DSB repair. However, paraspeckles do not colocalize with sites of ionizing radiation (IR)-induced DSBs (Supplementary Fig. 7a), suggesting that any influence of paraspeckles on DSB repair is indirect. Notably, and in contrast to previous reports^{43–48}, we found that all three RNA-binding proteins of the *Drosophila* DBHS family (SFPQ, NONO-p54nrb and PSPC1), which are all recruited to and essential components of paraspeckles, are excluded from sites of laser-induced DSBs (Supplementary Fig. 7b). On the basis of these observations, we propose that paraspeckles may contribute indirectly to DSB repair by sequestering DBHS, and possibly other, RNA-binding proteins away from DNA breaks to enable efficient recruitment of the DNA-repair machinery. Consistent with this possibility, it has been observed that transcription is interrupted at sites of damage and that RNA-binding proteins are rapidly excluded from these sites to allow efficient repair^{49–51}.

Neat1 KO mice do not show the phenotypes typically associated with deficiency in genes required for programmed DSB repair, such as growth retardation, progeria or defects in lymphocyte development⁵². Paraspeckles are therefore required for cell survival only under specific physiological conditions^{53,54} and, as shown here, in cells undergoing replication stress. This finding offers a unique opportunity to develop therapeutic modalities that are cancer-cell specific. The deficiency of cancer cells to respond to S-phase checkpoint activation could provide a basis for development of anticancer therapies that increase this vulnerability without affecting normal cells. *NEAT1* targeting exacerbates the sensitivity of cancer cells to DNA-damaging agents such as doxorubicin or platinum compounds. Moreover, and as expected if *NEAT1* and p53 are engaged in a negative feedback loop, *NEAT1* targeting is also synthetic lethal with nongenotoxic reactivation of p53. These data indicate that a wide range of human cancers may benefit from *NEAT1* targeting, as this approach can sensitize tumors expressing WT or mutant p53 to specific combination therapies. Given the recent surge of interest in RNA-targeting therapeutics and antisense drugs in particular, this therapeutic strategy may be rapidly amenable to the clinic.

METHODS

Methods and any associated references are available in the [online version of the paper](#).

Note: Any Supplementary Information and Source Data files are available in the online version of the paper.

ACKNOWLEDGMENTS

We thank O. Van Goethem, G. Bervoets and S. Peeters for excellent technical assistance; E. Bonomi and M. Bugatti (Fondazione Beretta) for ISH analysis of human cancer samples; and S. Jackson for helpful comments on the manuscript and for imaging facility access. Imaging was done on a Nikon A1 confocal microscope acquired through a Hercules grant type 1 (AKUL/09/037) to W. Annaert. This work was supported by Interuniversitaire Attractiepolen (IUAP), an Institute for Science, Innovation and Technology (IWT) scholarship to C.A. and a Fund for Scientific Research Flanders (FWO) scholarship to L.S. W.V. is supported by Associazione Italiana per la Ricerca sul Cancro (AIRC, IG 15378) and by Ministero Salute (RF-2010-2315888).

AUTHOR CONTRIBUTIONS

C.A., L.S. and J.B. designed and conducted experiments and acquired, analyzed and interpreted the data. M.L. performed DMBA and TPA treatments and monitored tumor development. A.V. and S.A. performed p53 ChIP-seq and RNA-seq experiments and data analysis. P.K. assessed DNA damage repair efficacy with bleomycin. B. Boeckx and D.L. analyzed expression data and constructed KM curves. E.R. and J.v.d.O. provided mouse and human pathology support. J.v.d.O. provided clinical samples. A.A.S., C.B. and E.L. designed research studies and contributed to interpretation of the data. G.L. and B. Beck provided reagents from mouse skin tumors. S.N. and T.H. provided *Neat1* KO mice. W.V. performed the TMA. P.W.G.W. provided reagents and contributed to interpretation of the data. All authors read and edited the manuscript. J.-C.M. designed research studies and wrote the manuscript.

COMPETING FINANCIAL INTERESTS

The authors declare no competing financial interests.

Reprints and permissions information is available online at <http://www.nature.com/reprints/index.html>.

- Vogelstein, B., Lane, D. & Levine, A.J. Surfing the p53 network. *Nature* **408**, 307–310 (2000).
- Sharpless, N.E. & DePinho, R.A. How stem cells age and why this makes us grow old. *Nat. Rev. Mol. Cell Biol.* **8**, 703–713 (2007).
- Vassilev, L.T. *et al.* In vivo activation of the p53 pathway by small-molecule antagonists of MDM2. *Science* **303**, 844–848 (2004).
- Khoo, K.H., Verma, C.S. & Lane, D.P. Drugging the p53 pathway: understanding the route to clinical efficacy. *Nat. Rev. Drug Discov.* **13**, 217–236 (2014).
- Carvajal, L.A. & Manfredi, J.J. Another fork in the road—life or death decisions by the tumour suppressor p53. *EMBO Rep.* **14**, 414–421 (2013).
- Huang, B., Deo, D., Xia, M. & Vassilev, L.T. Pharmacologic p53 activation blocks cell cycle progression but fails to induce senescence in epithelial cancer cells. *Mol. Cancer Res.* **7**, 1497–1509 (2009).
- Derrien, T. *et al.* The GENCODE v7 catalog of human long noncoding RNAs: analysis of their gene structure, evolution, and expression. *Genome Res.* **22**, 1775–1789 (2012).
- Yildirim, E. *et al.* *Xist* RNA is a potent suppressor of hematologic cancer in mice. *Cell* **152**, 727–742 (2013).
- Arun, G. *et al.* Differentiation of mammary tumors and reduction in metastasis upon *Malat1* lncRNA loss. *Genes Dev.* **30**, 34–51 (2016).
- Huarte, M. *et al.* A large intergenic noncoding RNA induced by p53 mediates global gene repression in the p53 response. *Cell* **142**, 409–419 (2010).
- Hung, T. *et al.* Extensive and coordinated transcription of noncoding RNAs within cell-cycle promoters. *Nat. Genet.* **43**, 621–629 (2011).
- Marin-Béjar, O. *et al.* Pint lincRNA connects the p53 pathway with epigenetic silencing by the Polycomb repressive complex 2. *Genome Biol.* **14**, R104 (2013).
- Blume, C.J. *et al.* p53-dependent non-coding RNA networks in chronic lymphocytic leukemia. *Leukemia* **29**, 2015–2023 (2015).
- Janky, R. *et al.* iRegulon: from a gene list to a gene regulatory network using large motif and track collections. *PLoS Comput. Biol.* **10**, e1003731 (2014).
- Herrmann, C., Van de Sande, B., Potier, D. & Aerts, S. i-cisTarget: an integrative genomics method for the prediction of regulatory features and cis-regulatory modules. *Nucleic Acids Res.* **40**, e114 (2012).
- Clemson, C.M. *et al.* An architectural role for a nuclear noncoding RNA: NEAT1 RNA is essential for the structure of paraspeckles. *Mol. Cell* **33**, 717–726 (2009).
- Wilusz, J.E. *et al.* A triple helix stabilizes the 3' ends of long noncoding RNAs that lack poly(A) tails. *Genes Dev.* **26**, 2392–2407 (2012).
- Chen, L.-L. & Carmichael, G.G. Altered nuclear retention of mRNAs containing inverted repeats in human embryonic stem cells: functional role of a nuclear noncoding RNA. *Mol. Cell* **35**, 467–478 (2009).
- Sasaki, Y.T.F., Ideue, T., Sano, M., Mityama, T. & Hirose, T. MENepsilon/beta noncoding RNAs are essential for structural integrity of nuclear paraspeckles. *Proc. Natl. Acad. Sci. USA* **106**, 2525–2530 (2009).
- Sunwoo, H. *et al.* MEN-epsilon nuclear-retained non-coding RNAs are up-regulated upon muscle differentiation and are essential components of paraspeckles. *Genome Res.* **19**, 347–359 (2009).
- Yamazaki, T. & Hirose, T. The building process of the functional paraspeckle with long non-coding RNAs. *Front. Biosci. (Elite Ed.)* **7**, 1–41 (2015).
- Reinhardt, H.C. & Schumacher, B. The p53 network: cellular and systemic DNA damage responses in aging and cancer. *Trends Genet.* **28**, 128–136 (2012).
- Nassar, D., Latil, M., Boeckx, B., Lambrechts, D. & Blanpain, C. Genomic landscape of carcinogen-induced and genetically induced mouse skin squamous cell carcinoma. *Nat. Med.* **21**, 946–954 (2015).
- Lapouge, G. *et al.* Identifying the cellular origin of squamous skin tumors. *Proc. Natl. Acad. Sci. USA* **108**, 7431–7436 (2011).
- Nakagawa, S., Naganuma, T., Shioi, G. & Hirose, T. Paraspeckles are subpopulation-specific nuclear bodies that are not essential in mice. *J. Cell Biol.* **193**, 31–39 (2011).
- Gaillard, H., García-Muse, T. & Aguilera, A. Replication stress and cancer. *Nat. Rev. Cancer* **15**, 276–289 (2015).
- Llopi, A. *et al.* The stress-activated protein kinases p38alpha/beta and JNK1/2 cooperate with Chk1 to inhibit mitotic entry upon DNA replication arrest. *Cell Cycle* **11**, 3627–3637 (2012).
- Branzei, D. & Foiani, M. Maintaining genome stability at the replication fork. *Nat. Rev. Mol. Cell Biol.* **11**, 208–219 (2010).
- Dobbelstein, M. & Sørensen, C.S. Exploiting replicative stress to treat cancer. *Nat. Rev. Drug Discov.* **14**, 405–423 (2015).
- Sullivan, K.D. *et al.* ATM and MET kinases are synthetic lethal with nongenotoxic activation of p53. *Nat. Chem. Biol.* **8**, 646–654 (2012).
- Ferriss, J.S. *et al.* Multi-gene expression predictors of single drug responses to adjuvant chemotherapy in ovarian carcinoma: predicting platinum resistance. *PLoS One* **7**, e30550 (2012).
- The Cancer Genome Atlas Research Network (TCGA). Integrated genomic analyses of ovarian carcinoma. *Nature* **474**, 609–615 (2011).
- Chakravarty, D. *et al.* The oestrogen receptor-alpha-regulated lncRNA NEAT1 is a critical modulator of prostate cancer. *Nat. Commun.* **5**, 5383 (2014).
- Choudhry, H. *et al.* Tumor hypoxia induces nuclear paraspeckle formation through HIF-2alpha dependent transcriptional activation of NEAT1 leading to cancer cell survival. *Oncogene* **34**, 4482–4490 (2015).
- Zhen, L. *et al.* Long noncoding RNA NEAT1 promotes glioma pathogenesis by regulating miR-449b-5p/c-Met axis. *Tumour Biol.* **37**, 673–683 (2016).
- Guo, S. *et al.* Clinical implication of long non-coding RNA NEAT1 expression in hepatocellular carcinoma patients. *Int. J. Clin. Exp. Pathol.* **8**, 5395–5402 (2015).
- Pan, L.-J. *et al.* Upregulation and clinicopathological significance of long non-coding NEAT1 RNA in NSCLC tissues. *Asian Pac. J. Cancer Prev.* **16**, 2851–2855 (2015).
- Sengupta, S. & Harris, C.C. p53: traffic cop at the crossroads of DNA repair and recombination. *Nat. Rev. Mol. Cell Biol.* **6**, 44–55 (2005).
- Harris, S.L. & Levine, A.J. The p53 pathway: positive and negative feedback loops. *Oncogene* **24**, 2899–2908 (2005).
- Cha, H. *et al.* Wip1 directly dephosphorylates gamma-H2AX and attenuates the DNA damage response. *Cancer Res.* **70**, 4112–4122 (2010).
- Moon, S.-H. *et al.* Wild-type p53-induced phosphatase 1 dephosphorylates histone variant gamma-H2AX and suppresses DNA double strand break repair. *J. Biol. Chem.* **285**, 12935–12947 (2010).
- Chowdhury, D. *et al.* gamma-H2AX dephosphorylation by protein phosphatase 2A facilitates DNA double-strand break repair. *Mol. Cell* **20**, 801–809 (2005).
- Rulten, S.L. *et al.* PARP-1 dependent recruitment of the amyotrophic lateral sclerosis-associated protein FUS/TLN1 to sites of oxidative DNA damage. *Nucleic Acids Res.* **42**, 307–314 (2014).
- Krietsch, J. *et al.* PARP activation regulates the RNA-binding protein NONO in the DNA damage response to DNA double-strand breaks. *Nucleic Acids Res.* **40**, 10287–10301 (2012).
- Ha, K., Takeda, Y. & Dynan, W.S. Sequences in PSF/SFPQ mediate radioresistance and recruitment of PSF/SFPQ-containing complexes to DNA damage sites in human cells. *DNA Repair (Amst.)* **10**, 252–259 (2011).
- Saiton, M., Lenthal, Y., Wang, S.Y., Chen, D.J. & Shiloh, Y. Involvement of Matrin 3 and SFPQ/NONO in the DNA damage response. *Cell Cycle* **9**, 1568–1576 (2010).
- Mastrocola, A.S., Kim, S.H., Trinh, A.T., Rodenkirch, L.A. & Tibbetts, R.S. The RNA-binding protein fused in sarcoma (FUS) functions downstream of poly(ADP-ribose) polymerase (PARP) in response to DNA damage. *J. Biol. Chem.* **288**, 24731–24741 (2013).
- Altmeyer, M. *et al.* Liquid demixing of intrinsically disordered proteins is seeded by poly(ADP-ribose). *Nat. Commun.* **6**, 8088 (2015).
- Wickramasinghe, V.O. & Venkataraman, A.R. RNA processing and genome stability: cause and consequence. *Mol. Cell* **61**, 496–505 (2016).
- Britton, S. *et al.* DNA damage triggers SAF-A and RNA biogenesis factors exclusion from chromatin coupled to R-loops removal. *Nucleic Acids Res.* **42**, 9047–9062 (2014).
- Shanbhag, N.M., Rafalska-Metcalf, I.U., Balane-Bolivar, C., Janicki, S.M. & Greenberg, R.A. ATM-dependent chromatin changes silence transcription in cis to DNA double-strand breaks. *Cell* **141**, 970–981 (2010).
- Specks, J., Lecona, E., Lopez-Contreras, A.J. & Fernandez-Capetillo, O. A single conserved residue mediates binding of the ribonucleotide reductase catalytic subunit RRM1 to RRM2 and is essential for mouse development. *Mol. Cell. Biol.* **35**, 2910–2917 (2015).
- Nakagawa, S. *et al.* The lncRNA Neat1 is required for corpus luteum formation and the establishment of pregnancy in a subpopulation of mice. *Development* **141**, 4618–4627 (2014).
- Standaert, L. *et al.* The long noncoding RNA Neat1 is required for mammary gland development and lactation. *RNA* **20**, 1844–1849 (2014).

ONLINE METHODS

Cell culture. All cell lines were acquired from the LCG ATCC Cell Biology collection and kept in culture at 37 °C and 5% CO₂ in medium supplemented with 1% penicillin and streptomycin (Invitrogen) and 10% FBS (Invitrogen). None of the cell lines used were reported in the ICLAC database of commonly misidentified cell lines. All cell lines were tested monthly for mycoplasma contamination and found negative. After their initial purchase, cell lines were not further authenticated. For knockdown experiments with locked nucleic acid (LNA)-GapmeRs (Exiqon), cells were transfected using Lipofectamine 2000 (Thermo Fisher Scientific) with a final concentration of 25 nM GapmeR and transfection reagent according to the manufacturer's instructions. *NEAT1*-specific sequences were 5'-TAAGCACTTTGGAAAG-3' (N1) and 5'-CTCACACGTCATCT-3' (N1_2), and a validated nontargeting oligonucleotide 5'-TCATACTATATGACAG-3' was used as a control. For knockdown experiments with siPOOLS (siTOOLS Biotech), 30 nM siRNA was transfected using Lipofectamine RNAiMAX (Thermo Fisher Scientific).

Mice. *Neat1* KO, p53 KO and WT mice were maintained on a pure C57BL/6J background in a certified animal facility. All animal experiments were carried out in accordance with the guidelines of the University of Leuven Animal Care and Use ethical Committee under project license 089/2013. *Neat1* and *Tp53* KO mice were described previously^{25,55}. K14 CreER KRas^{G12D} have been previously described⁵⁶. For chemically induced carcinogenesis with DMBA (D3254, Sigma-Aldrich) and phorbol 12-myristate 13-acetate (TPA) (P8139, Sigma-Aldrich), cohoused 4- to 8-week-old mice were treated as previously described⁵⁷. For the short-term experiments, mice were sacrificed at the indicated time points. For the long-term tumor formation assay, mice were sacrificed when the tumors exceeded a diameter of 10 mm or showed significant cachexia (weight loss ≥ 20%), or when > 50% of WT mice had reached those end points. WT and *Neat1* KO littermates were randomly assigned to each of the experiments irrespective of their gender. Owing to limited numbers of animals, no power testing was performed before the start of the experiments. The size of each group was determined by the number of animals at our disposal at the time of the experiment; *n* ≥ 3 mice per group for all experiments.

Quantitative real-time reverse transcription PCR. Total RNA was isolated using the NucleoSpin RNA/Protein kit (740933.50, Machery-Nagel) or the RNeasy Mini kit (74104, Qiagen) according to the manufacturer's instructions. RNA was quantified with a NanoDrop 1000 (Thermo Scientific) and RNA was reverse transcribed using the High-Capacity cDNA reverse transcription kit (4368814, Applied Biosystems). Quantitative reverse-transcription PCR (RT-qPCR) was performed using Fast SYBR Green 2× master mix according to the manufacturer's instructions (4385612, Applied Biosystems). For normalization, the geometric mean of the two most stable reference genes out of at least three was used, calculated using geNorm. Real-time PCRs were carried out in a Roche LightCycler-480-384. RT-qPCR primer sequences were as follows: *NEAT1_1* fw: 5'-GGAGAGGGTTGGTTAGAGAT-3'; *NEAT1_1* rev: 5'-CCTTCAACCTGCATTCCTA-3'; *NEAT1_2* fw: 5'-GGCCAGAGCTTTGTTGCTTC-3'; *NEAT1_2* rev: 5'-GGTGGGGCACTTACTTACT-3'; *UBC* fw: 5'-ATTTGGGTCGCGGTTCTT-3'; *UBC* rev: 5'-TGCCTTGACATTTCTCG ATGGT-3'; *TBP* fw: 5'-CGGCTGTTAACTTCGCTTC-3'; *TBP* rev: 5'-CACACG CCAAGAAACAGTGA-3'; *B2M* fw: 5'-TGCTGTCTCCATGTTTGATGTATCT-3'; *B2M* rev: 5'-TCTCTGCTCCACCTCTAAGT-3'; *HPRT1* fw: 5'-TGACA CTGGCAAAACAATGCA-3'; *HPRT1* rev: 5'-GGTCTTTTACCAGCAA GCT-3'; *mNeat1_2* fw 5'-GCTCTGGGACCTTCGTGACTCT-3'; *mNeat1_2* rev 5'-CTGCCTTGGCTTGGAAATGTAA-3'; *mNeat1* fw 5'-TTGGGA CAGTGGACGTGTGG-3'; *mNeat1* rev 5'-TCAAGTGCCAGACAGACAGCA-3'; *mHmbs* fw 5'-GCGGAGTCATGTCCGGTAA-3'; *mHmbs* rev 5'-GTGGTG GACATAGCAATGATTT-3'; *mGapdh* fw 5'-AGGTTGTCTCCTGCGAC TTCA-3'; *mGapdh* rev 5'-GGTGGTCCAGGGTTTCTTACTC-3'.

Immunoblotting. Cells were scraped on ice in RIPA buffer containing protease and phosphatase inhibitor cocktails (Thermo Fisher, 78442). The cell lysates were five times pushed through a 22-gauge needle with syringe and vortexed, incubated on ice for 10 min and then centrifuged at 21,000 × *g* for 15 min at 4 °C. For western blotting, 20 µg total protein lysate was loaded on NuPAGE

Novex 4–12% Bis-Tris Protein Gels (Invitrogen) and probed with the following antibodies: phosphoKAP-1 (S824) (Bethyl Laboratories, A300-767A, 1/1,000); KAP1 (BD Biosciences, 610334, 1/1,000); histone H2A.X (p-Ser139) (Millipore, 05-636, 1/1,000) and GAPDH (Abcam, ab9485, 1/1,000), ATR (N-19) (Santa Cruz, sc-1887, 1/200), p-S345 Chk1 (Cell Signaling, 133D3, 1/1,000), total Chk1 (G4) (Santa Cruz, sc-8408, 1/1,000), p-S33 RPA32 (9H8) (Bethyl Laboratories, A300-246A, 1/1,000), total RPA32 (9h8) (Abcam, ab2175, 1/1,000), total H2A.X (Abcam, ab11175, 1/5,000).

Cell growth assays. Cells were seeded and transfected in 96-well plates at a concentration of 3,000 cells per well. At different time points, WST1 reagent was added according to the manufacturer's instructions (Roche, 05 015 944 001) and luminescence was measured with VICTOR X3 Multilabel Plate Reader (PerkinElmer).

Long-term growth assays. 24 h after transfection, cells were counted and seeded for the long-term growth assay. 24 h after seeding, cells were treated with a 1-h pulse of 2.5 µM doxorubicin (Sigma-Aldrich), or with a constant dose of either 80 µM ABT-888 PARP inhibitor (Enzo Life Sciences, ALX-270-444-M001) or 5 µM Nutlin-3a (Roche). After 4 or 7 d in culture (5–8 d after transfection), colonies were stained with crystal violet (Sigma-Aldrich) and quantified using ImageJ software.

FACS analysis. To detect cell death, cells were stained for 15 min with Annexin V and PI using the FITC Annexin V Apoptosis Detection Kit II (BD Biosciences) according to the manufacturer's instructions. Cell death was detected on a BD FACSCanto (BD Biosciences), and data were analyzed with FlowJo software (Tree Star). For cell cycle distribution analysis in *NEAT1_2* KD conditions, cells were treated with vehicle or 1 mM HU for 5 h 48 h after transfection and pulsed for 30 min with 10 µM EdU. After trypsinization and washing once in cold PBS, cells were fixed for 20 min in 2% PFA in PBS. They were washed with PBS + 1 mg/ml BSA (PBS-B) and permeabilized with PBS + 0.02% Triton X-100 for 20 min then washed again with PBS-B. Subsequently, the cells were spun down and resuspended in the Click-reaction cocktail (per sample: 43.75 µl PBS, 1 µl 100 mM CuSO₄, 0.25 µl 200 µM azide dye and 5 µl 100 mM sodium ascorbate), incubated for 40 min, washed in PBS-B, resuspended in 0.5 ml PBS containing 0.5 µg/ml DAPI and analyzed on a BD FACS Canto. Data were analyzed using FlowJo software (Tree Star).

RNA-seq. MCF-7 cells were plated onto 24-well plates (60,000 cells/well). The next day, cells were treated with either 5 µM Nutlin-3a or ethanol vehicle. After 24 h, cells were washed in PBS (Gibco) and prepared for RNA extraction according to the RNeasy protocol (Qiagen), which yielded ~2 µg of total RNA per sample. The quality of the RNA samples was checked using a Bioanalyzer 1000 DNA chip (Agilent), after which libraries were constructed according to the Illumina TruSeq RNA sample preparation guide. Final libraries were pooled and sequenced on a HiSeq 2000 (Illumina), generating approximately 30 million reads of 50 bp in length. After removing adaptor sequences, reads were mapped to the human reference genome (hg19) using TopHat v1.3.3 (ref. 58) with default settings. Reads were aggregated with HT-Seq⁵⁹ (-str = no parameter, version 0.5.3p3) using the human Gencode annotation V18 (ref. 60), lncRNAs only. DESeq⁶¹ was used to normalize and to calculate differential expression between Nutlin-3a-stimulated and unstimulated samples. A final list of differentially expressed genes was obtained using adjusted *P* value < 0.05 and |log₂FC| > 1. The RNA-seq data are available in the GEO database (GEO GSE47043).

ChIP-seq. MCF-7 cells were seeded at a density of 5 million cells per 15-cm dish to ~80% confluency and grown overnight at 37 °C. Cells were stimulated with 5 µM Nutlin-3a for 24 h. ChIP samples were prepared following the Magna ChIP-Seq preparation kit using the p53 antibody (DO-1, SCBT, 1 µg/sample). Per sample, 5–10 ng of precipitated DNA was used to perform library preparation according to the Illumina TruSeq DNA sample preparation guide. In brief, the immunoprecipitated DNA was end-repaired, A-tailed, and ligated to diluted sequencing adaptors (dilution of 1/100). After PCR amplification with 15–18 cycles and gel size selection of 200- to 300-bp fragments, the libraries were sequenced using the HiSeq 2000 (Illumina). Cleaned reads were mapped to the

human reference genome hg19 (UCSC) using bowtie (v2.0.0-beta3) with the addition of the parameter *-local*, allowing for further soft clipping of the reads. Reads with a mapping quality <4 were removed. Peak calling was performed using MACS⁶² (version 1.4.2) with the default *P* value threshold yielding 3,634 peaks. The ChIP-seq data are available in the GEO database (GEO GSE47043).

Motif discovery and network analysis. To detect putative p53 binding sites we adapted the *i-cisTarget* method¹⁵. In short, a region of 10 kb flanking the TSS of each lncRNA (GENCODE annotation V18) was scored for 6,863 different position weight matrices (PWM), representing a large collection of transcription factors. This led to a ranking of all lncRNAs for each of these PWMs. Next, for each PWM we retrieved the rank position of all upregulated lncRNAs and calculated an enrichment score for this set using the normalized area under the recovery curve, as described¹⁵. This score recapitulates how many of the upregulated lncRNAs are enriched at the top of the ranking for a particular PWM and whether this enrichment is significantly higher than expected by chance. From this analysis we selected the PWM with the highest enrichment score across all 6,863 PWMs, namely *TP53*. Next, we determined the optimal set of p53 targets as the rank position in the p53 ranking where the cumulative recovery of upregulated lncRNAs is highest compared to the background (i.e., the average recovery across all PWM rankings). For each predicted target lncRNA, we searched for p53 ChIP-peaks within 10 kb of the TSS of each lncRNA. If multiple peaks were detected, the one with the highest score was selected. The final network was generated using Cytoscape v2.8.2 (ref. 63).

Kaplan–Meier curve construction. The correlation of *NEAT1* expression levels with response to chemotherapy was evaluated in two data sets of ovarian tumors (TCGA ovarian data set and GSE30161). We selected ovarian carcinoma because all the patients were treated with platinum-based chemotherapy. The TCGA ovarian data set was generated by poly(A)-based RNA sequencing, in which specific expression of the non-polyadenylated long *NEAT1* isoforms is not available. This data set was extended with in-house-sequenced ovarian tumors and primary, high-grade, serous, platinum sensitive tumors with a recurrence, excluding the patients with Fédération Internationale de Gynécologie et d'Obstétrique (FIGO) I, were selected. In addition, we assessed the Affymetrix Human Genome U133 Plus 2.0 Array data set to discriminate the effect of the long and short isoform of *NEAT1* on the response of chemotherapy. This microarray has probes (227062_at, 234989_at, 238320_at, 225239_at and 239269_at) that specifically detect the long *NEAT1* isoform, whereas probes 224565_at, 224566_at and 214657_s_at detect both the short and long isoforms of *NEAT1*. Data set GSE30161 consists of 58 high-grade ovarian tumors that all received platinum therapy. A Cox survival analysis of low and high *NEAT1* expression levels was performed on both data sets including race, stage, age and histology as covariates (for GSE30161) and grade, residual disease, FIGO and race for the extended TCGA data set. Kaplan–Meier curves were generated and Cox regression analyses were performed using the survival package in R 3.2.1.

Tissue staining and image quantification. For histological analysis, mouse back skin was dissected, spread on Whatman cellulose filter paper, fixed for 2 or 24 h in 4% PFA in PBS and processed for OCT or paraffin embedding, respectively. Samples were sectioned at 5–7 μ m and routinely stained with hematoxylin (C0302, Diapath) and eosin (C0362, Diapath) (H&E). Serial sections obtained from the same samples were used for immunohistochemical analysis using the following primary antibodies: rabbit polyclonal anti-pH3 (Calbiochem, 382159; 1/200), chicken polyclonal anti-keratin 14 (Abcam, 13970; 1/1,000), rabbit polyclonal anti-p53 (Santa Cruz, sc-6243; 1/1,500), rabbit polyclonal anti-Ki67 (Thermo Scientific RM-9106-S, clone SP6; 1/300), rabbit polyclonal anti- γ -H2A.X (Cell Signaling, 2577; 1/1,400), rabbit polyclonal anti-cleaved caspase 3 (Cell Signaling, Asp175; 1/600), rat monoclonal anti-BrdU (Abcam, ab6326; 1/1,500), rabbit polyclonal anti-keratin 5 (Covance, PRB-160P-0100; 1/1,000). For immunofluorescence, anti-rabbit or rat IgG-A488 or A594 (Life Technologies, 1/500) and anti-chicken-IgG-RXX (Elitech, 703-295-155, 1/1,000) secondary antibodies were used.

For immunohistochemical (IHC) staining, sections were deparaffinized in xylene and rehydrated using an ethanol series. Endogenous peroxidase activity was blocked by 15 min incubation with 3–4% H₂O₂ (Perdrogen, 31642,

Sigma-Aldrich) in dH₂O. Epitope retrieval was performed in citrate buffer (pH6) or EDTA buffer (pH 8.5, p53 antibody) using a 2100 Retriever (Aptum Biologics). The sections were blocked in 1% BSA and 10% NGS for 40 min at room temperature (RT) and incubated overnight at 4 °C with the primary antibody in 1% BSA in T-TBS. EnVision reagent (K400311, Dako) was then applied on the sections for 45 min at RT. Immunoreactivity was revealed via a diaminobenzidine chromogen reaction (Peroxidase Substrate Kit, DAB, SK-4100, Vector Laboratories). Next, slides were counterstained in hematoxylin, dehydrated in an ethanol series, cleared in xylene, and permanently mounted with a resinous mounting medium (60200, Micromount Diapath). A 0.1% Tween-20 in TBS solution was used as washing buffer in between steps. For immunofluorescence staining, the same procedure was followed but with blocking in 10% NDS, use of fluorescently labeled anti-rabbit, mouse and chicken secondary antibodies (Life Technologies, 1/500), nuclear counterstaining with DAPI and mounting with VectaShield (H-1000, Vector Laboratories). For proliferation analysis with BrdU, 5 μ l/g of a 20 mg/ml BrdU solution was injected intraperitoneally 4 h before sacrifice.

To quantify IHC staining, 5 hotspot brightfield images per mouse were taken with a Leica DM 2500 microscope at 20 \times magnification, and positive cells in the interfollicular epidermis and infundibulum of hair follicles were counted and normalized to the total length of the epidermis measured at the basal layer in the image. Counting of total number of individual cells in the same area gave near-identical normalized results. For quantification of fluorescent images, a similar approach was used employing 20 \times magnified images taken with a Leitz DMRB microscope. LAS software (Leica Microsystems) was used for all IHC and IF image acquisition. Quantification of hyperplasia in **Figure 4b** was done in H&E-stained sections (6 images per mouse at 10 \times magnification) by calculating the ratio of the total length of each category of epidermal thickness (1–2, 3–4, 5–7 and >7 cell layers) to the total length of the epidermal tract analyzed. All measures or quantifications and analyses were performed by two observers blind to genotype and treatment. Exclusion was based on the Grubbs test for outlier calculation with $\alpha = 0.05$; however, no significant outliers were detected during the analysis. To determine differences in variance of the groups, an F-test was performed with $\alpha = 0.05$. If the variances showed to be different, the Welch-corrected *P* value was represented. Validation of all antibodies used in this study is available on the manufacturer's websites.

RNA–fluorescence *in situ* hybridization. *NEAT1* RNA–FISH was performed using Stellaris FISH probes (human, SMF-2036-1; mouse, SMF-3010-1) according to the manufacturer's protocol. In brief, after deparaffinization and rehydration, the tissue was immersed in 70% ethanol for >1 h at room temperature, washed in PBS, digested with 10 μ g/ml proteinase K in PBS, preincubated in wash buffer and hybridized overnight at 37 °C. The next day, the tissue was washed extensively, counterstained with DAPI and mounted with Vectashield Anti-Fade mounting medium (Vector Laboratories). For cryosections and human cells, no proteinase K digestion was performed. For simultaneous immunofluorescence, the following primary antibodies were used together with the FISH probes: rabbit polyclonal anti-keratin 5 (Covance, PRB-160P, 1/1,000) or rabbit polyclonal anti-keratin 1 (Covance, PRB-165P, 1/1,000). Secondary antibodies coupled to Alexa 488 (1/500, Life Technologies) were added to the first washing step after hybridization for 40 min at 37 °C. Images were taken using a Nikon A1 confocal microscope acquired through a Hercules grant type 1 AKUL/09/037 and processed for overlay and brightness and contrast adjustments using ImageJ. Red-channel images (**Fig. 2e**) were smoothed once for aesthetic enhancement of the paraspeckles. Paraspeckle quantification in cell lines was automated and used IN Cell Analyzer 2000 (GE Healthcare Life Sciences) and IN Cell Developer software (GE Healthcare Life Sciences). Paraspeckle quantification in tissues was done by taking 6 images per mouse at a 60 \times magnification and counting the numbers of nuclei with paraspeckles in proportion to the total number of nuclei in all layers of the interfollicular epidermis.

Tissue microarray (TMA). Formalin-fixed paraffin-embedded (FFPE) tissue blocks were retrieved from the tissue bank of the Department of Pathology, Spedali Civili di Brescia, Brescia, Italy. Human tissues included normal tonsils as controls, whereas pathological samples included multitumor tissue microarrays (TMA) of mixed carcinomas. TMA blocks were obtained from a series of 97

primary carcinomas (PC) from different sites and constructed using an automated tissue microarrayer (TMA Master, 3DHistech). Three representative tumor areas were identified on H&E-stained sections. For each area, a 1-mm core was obtained by punching the original tissue block. 4- μ m-thick tissue sections were H&E stained and checked for tumor cell content. Sections and stainings on TMA were performed as described above. Slides were examined using an epifluorescence microscope (Nikon, Eclipse 90I) with appropriate filters for SpectrumOrange and a UV filter for the DAPI nuclear counterstain.

55. Jacks, T. *et al.* Tumor spectrum analysis in p53-mutant mice. *Curr. Biol.* **4**, 1–7 (1994).
56. Vasioukhin, V. *et al.* The magical touch: genome targeting in epidermal stem cells induced by tamoxifen application to mouse skin. *Proc. Natl. Acad. Sci. USA* **96**, 8551–8556 (1999).

57. Abel, E.L., Angel, J.M., Kiguchi, K. & DiGiovanni, J. Multi-stage chemical carcinogenesis in mouse skin: fundamentals and applications. *Nat. Protoc.* **4**, 1350–1362 (2009).
58. Trapnell, C., Pachter, L. & Salzberg, S.L. TopHat: discovering splice junctions with RNA-seq. *Bioinformatics* **25**, 1105–1111 (2009).
59. Anders, S., Pyl, P.T. & Huber, W. HTSeq—a Python framework to work with high-throughput sequencing data. *Bioinformatics* **31**, 166–169 (2015).
60. Harrow, J. *et al.* GENCODE: the reference human genome annotation for The ENCODE Project. *Genome Res.* **22**, 1760–1774 (2012).
61. Anders, S. & Huber, W. Differential expression analysis for sequence count data. *Genome Biol.* **11**, R106 (2010).
62. Zhang, Y. *et al.* Model-based analysis of ChIP-Seq (MACS). *Genome Biol.* **9**, R137 (2008).
63. Smoot, M.E., Ono, K., Ruscheinski, J., Wang, P.L. & Ideker, T. Cytoscape 2.8: new features for data integration and network visualization. *Bioinformatics* **27**, 431–432 (2011).